An adaptive meshfree method for phase-field models of biomembranes. Part I: approximation with maximum-entropy approximants

A. Rosolen[☆], C. Peco and M. Arroyo[*]

LaCàN, Universitat Politècnica de Catalunya-BarcelonaTech (UPC), Barcelona 08034, Spain

Abstract

We present an adaptive meshfree method to approximate phase-field models of biomembranes. In such models, the Helfrich curvature elastic energy, the surface area, and the enclosed volume of a vesicle are written as functionals of a continuous phase-field, which describes the interface in a smeared manner. Such functionals involve up to second-order spacial derivatives of the phase-field, leading to fourth-order Euler-Lagrange partial differential equations (PDE). The solutions develop sharp internal layers in the vicinity of the putative interface, and are nearly constant elsewhere. Thanks to the smoothness of the local maximum-entropy (*max-ent*) meshfree basis functions, we approximate numerically this high-order phase-field model with a direct Ritz-Galerkin method. The flexibility of the meshfree method allows us to easily adapt the grid to resolve the sharp features of the solutions. Thus, the proposed approach is more efficient than common tensor product methods (e.g. finite differences or spectral methods), and simpler than unstructured C^0 finite element methods, applicable by reformulating the model as a system of second-order PDE. The proposed method, implemented here under the assumption of axisymmetry, allows us to show numerical evidence of convergence of the phase-field solutions to the sharp interface limit as the regularization parameter approaches zero. In a companion paper, we present a Lagrangian method based on the approximants analyzed here to study the dynamics of vesicles embedded in a viscous fluid.

Keywords: maximum-entropy approximants, meshfree methods, adaptivity, phase field models, biomembranes, vesicles.

1. Introduction

Biomembranes are the fundamental separation structure in animal cells, and are responsible for the compartmentalization of the cell or for the transport of substances through cargo vesicles or tubes. They also play a key role in bio-mimetic engineered systems [1]. Their complex behaviour, rich physical properties, formation and dynamics have been objects of experimental and theoretical investigation for biologists, chemists and physicists during many years [2, 3]. Biomembranes are composed by several kinds of lipids self-assembled in a fluid bilayer, which

[☆]Current address: Institute for Soldier Nanotechnologies, MIT, Cambridge MA, USA.

[*]Correspondence to: marino.arroyo@upc.edu

presents a liquid behaviour in-plane and solid out-of-plane [4]. Vesicles are closed biomembranes, which play an important role in biophysical processes such as in the delivery of proteins, antibodies or drugs into cells, and separation of different types of biological macromolecules within cells. Vesicles serve as simplified models of more complex biological systems, and can be used to study the interaction between lipid bilayers and the surrounding medium, e.g. under osmotic stress [5], shear flow [6], or electrical fields [7]. Depending on the lipid composition, lipid bilayers can phase-separate forming multicomponent vesicles [8], which have also been the object of numerous studies as model systems for rafts.

Lipid bilayers can be modeled by very different techniques, depending on the focus. Atomistic [9] and coarse-grained [10] molecular dynamics (MD) can access molecular processes and the self-assembly. However, due to the slow relaxation of the bending modes, the computational cost of molecular simulations scales as L^6, where L is the lateral dimension of the system [11]. Even if coarse-grained MD simulations have been able to describe the collective dynamics of membrane patches of tens of nanometers, this sets a very stringent limit on the system sizes accessible with these methods. Other mesoscopic methods such as dynamically triangulated surfaces have been proposed to deal with intermediate scales [12]. On the other end of the spectrum, continuum mechanics has showed great success over the last decades in describing the equilibrium shapes of vesicles [4, 13, 14]. Continuum models have also helped understand the dynamics of fluctuations of bilayers [15], or the shape dynamics of membranes [16, 17]. Continuum mechanics models of biomembranes disregard atomic details, but still can incorporate many important effects such as the bilayer asymmetry, the spontaneous curvature, the diffusion of chemical species on the bilayer, or the dissipative mechanisms arising from the friction between the lipids [18]. Furthermore, these methods can easily access wide spans of time and length scales. The main drawback of these models is that they are usually formulated as complex nonlinear high-order partial differential equations (PDE). Here, we focus on the numerical approximation of a simple curvature model for biomembranes.

The Canham-Helfrich functional [19, 20] is a widely accepted continuum model for the curvature elasticity of fluid membranes, which explains to a large extent the observed morphologies of vesicles. This sharp interface model has been the basis of a number of numerical parametric approaches for the equilibrium analysis of axisymmetric and three-dimensional vesicles. The resulting equations for the parameterization are fourth-order nonlinear PDE. This functional is reparameterization invariant, which reflects mathematically the in-plane fluidity of lipid bilayers above the transition temperature. This feature poses numerical difficulties to parametric methods, since this invariance needs to be controlled to avoid serious mesh distortions [21, 22].

Phase-field counterparts of this model have been proposed and exercised numerically [23, 24, 25]. Although these methods increase the dimension of the problem, they naturally overcome the limitations of parametric methods when extreme shape, or even topology changes are present, and produce more robust simulations. Furthermore, these methods are more amenable to scalable parallel computations for complex systems, particularly when coupling it to the fluid mechanics of the ambient medium. Yet, the numerical solution of these models, again expressed mathematically as nonlinear fourth-order PDE, is challenging. Here, we propose to address high-order character of the equations and the sharp fronts they develop with an adaptive mesh-free method. We establish here the ability of the local maximum-entropy approximants [26]

to accurately and efficiently approximate equilibrium solutions of the phase-field model with a straight Ritz-Galerkin approach. In a companion paper [27], we propose a Lagrangian method to deal with the dynamics of vesicles embedded in a viscous fluid in the low Reynolds number limit, representative of most biological situations of interest.

The outline of the paper is as follows. Section 2 introduces the sharp interface and the phase-field models for the curvature elasticity of biomembranes, as well as a brief account of the numerical strategies to address these models. Section 3 describes the discretization of the phase-field functionals with the local maximum-entropy approximations schemes, the algorithm to find equilibrium solutions, and the method used to distribute the nodes. Numerical experiments to evaluate the performance of the approximants and the adaptive strategy are presented in Section 4. The final conclusions are collected in Section 5.

2. Sharp interface model, phase-field model, and its numerical treatment

2.1. Sharp interface model

In the sharp interface (S-I) approach, the membrane is a mathematical surface without thickness. The equilibrium shapes of vesicles minimize the Canham-Helfrich energy under area and enclosed volume constraints follow from

$$\begin{aligned} \text{(S-I model)} \qquad \text{Minimize} \quad & E(\Gamma) = \frac{k}{2}\int_\Gamma (H - C_0)^2 \; dS + k_G \int_\Gamma K \; dS \\ \text{subject to} \quad & V(\Gamma) = \frac{1}{3}\int_\Gamma \boldsymbol{x}\cdot\boldsymbol{n} \; dS = V_0 \\ & A(\Gamma) = \int_\Gamma dS = A_0, \end{aligned}$$

where Γ is the surface, k the bending rigidity, k_G the Gaussian bending rigidity, H the mean curvature, K the Gaussian curvature, $\boldsymbol{n}$ the normal to the surface, V_0 and A_0 are the prescribed volume and surface area, and C_0 is the spontaneous curvature. For surfaces of constant topology, the second integral in the curvature energy is a constant, and for this reason it is often ignored. We do not consider this term in the remainder of the paper, although is can be easily incorporated.

The area constraint comes from the near inextensibility of lipid bilayers under the usual applied forces. The volume can be regulated by osmotic effects, since biomembranes are semi-permeable. If the volume V_0 is smaller than the volume enclosed by a sphere of area A_0, then various equilibrium shapes are possible. For a given area and volume, there exist multiple equilibrium branches, as a consequence of the nonlinearity and non-convexity of the S-I model.

Various numerical methods have been proposed to solve the S-I model. Given the fact that the functional involves second derivatives of the parameterization, a direct Galerkin approach demands C^1 parameterizations. In 3D, this has been realized with subdivision finite elements [21, 28] and spherical harmonics [22]. Alternative formulations are amenable to C^0 finite elements [29, 30]. All these parametric approaches need to control the tangential motions of the mesh to avoid severe distortions.

2.2. Phase-field model

Phase-field models provide a powerful tool to tackle moving interface problems [31], and have been extensively used in physics and materials science (see [32, 33] and references therein). Recently, they are gaining popularity in a wide set of applications in applied science and engineering such as fracture [34, 35], microstructure formation and fracture evolution in ferroelectric materials [36], growth of thin films [37], image segmentation [38] and multi-phase flows [39], to mention a few.

The idea behind phase-field modeling is to replace the sharp description of the interface by a smeared continuous layer. To this end, an auxiliary field ϕ, called order parameter or phase-field, is introduced to represent the phases (e.g. inside and outside of the vesicle), and also the interface. The phase-field adopts distinct values, say -1 and +1, in each of the phases, and smoothly varies between these values in the diffuse interface. Typically, an energy functional expressed in terms of the phase-field models the physical phenomena at hand. Hence, the phase-field equation accomplishes two tasks at once: (1) it localizes the phase-field to represent a (smeared) interface, and (2) it encodes the interfacial physics. In sharp interface models, the geometric description of the interface is extrinsic to its physics.

The phase-field model for biomembranes proposed by Du *et al.* [23, 40] replaces the S-I model by:

$$
\begin{aligned}
\text{(P-F model)} \qquad \text{Minimize} \quad & E[\phi] = f_E \frac{k}{2\epsilon} \int_\Omega \left[\epsilon \Delta \phi + \left(\frac{1}{\epsilon}\phi + C_0\sqrt{2} \right) \left(1-\phi^2\right) \right]^2 \, d\Omega \\
\text{subject to} \quad & V[\phi] = \frac{1}{2}\left(Vol(\Omega) + \int_\Omega \phi \, d\Omega \right) = V_0 \\
& A[\phi] = f_A \int_\Omega \left[\frac{\epsilon}{2} |\nabla \phi|^2 + \frac{1}{4\epsilon}(\phi^2-1)^2 \right] \, d\Omega = A_0 \\
& \phi|_{\partial\Omega} = -1,
\end{aligned}
$$

where ϵ is a small regularization parameter, $f_E = \frac{3}{8\sqrt{2}}$, $f_A = \frac{3}{2\sqrt{2}}$, Ω is the domain bounding the vesicle, and $\partial\Omega$ its boundary. The regions $\{\boldsymbol{x} : \phi(\boldsymbol{x}) > 0\}$ and $\{\boldsymbol{x} : \phi(\boldsymbol{x}) < 0\}$ represent, the inside and outside of the membrane, while the level set $\{\boldsymbol{x} : \phi(\boldsymbol{x}) = 0\}$ can be used to realize the position of the membrane.

Formal asymptotics [40], as well as rigorous mathematical analysis [41] (see also [42] for a review), provide the connection between the P-F model and the S-I mode when $\epsilon \to 0$. As this limit is never achieved in the numerical calculations, a modeling error is always present in practice. This model has been coupled with the Navier-Stokes equations in [43]. Similar ideas to couple phase-field models of biomembranes with fluid or other physical fields have been developed by other researchers as well [7, 24, 44, 45].

2.3. Numerical approaches for the phase-field functionals

The main advantage of the phase-field model is the unified treatment of the interfacial tracking and the mechanics, which potentially leads to simple, robust, scalable computer codes. This comes at the expense of a much higher computational cost, particularly if the modeling error with respect to the sharp interface limit needs to be small. Indeed, in can be seen that

the phase-field model produces solutions with the profile $\phi(\boldsymbol{x}) = \tanh\left[\frac{d(\boldsymbol{x})}{\sqrt{2}\epsilon}\right]$, where $d(\boldsymbol{x})$ is the distance to the interface. Resolving this profile requires a very fine discretization for small values of ϵ, but this high resolution is only required in the vicinity of the interface. Away from it, the phase-field is nearly constant. Hence, this problem naturally calls for adaptivity. Furthermore, a numerical method for the phase-field model needs to address the second-order derivatives in the energy and area functionals.

Traditional numerical methodologies like finite difference [23, 44] and spectral methods [43] have been used for phase-field models of biomembranes. Recently, isogeometric analysis [46], a Galerkin method based on tensor products of 1D NURBS approximants, has shown an excellent performance for the Cahn-Hilliard equation, handling successfully the sharp transitions of the solutions without spurious overshoots [47, 48]. Although these structured methods can handle higher-order operators, they have difficulties in adapting to localized features. C^0 finite element approaches can deal with the high-order character of the functional by reformulating the model as a system of second-order PDE [49] and are well suited for adaptivity [50], but suffer from poor accuracy for a given computational cost. A number of adaptive techniques have been developed for the Cahn-Hilliard model, including an adaptive multigrid finite-difference method [51, 52], a Fourier spectral moving-mesh method [53], an adaptive FEM with linear [45, 54, 55] and quadratic [56] shape functions after recasting the higher-order phase-field as a system of lower-order equations, and a finite volume approach for unstructured grids [57]. Adaptive methods based on finite differences [58, 59], Fourier spectral [60], or finite volumes [61, 62] have been proposed for other higher-order phase-field equations.

Here, we propose a Ritz-Galerkin method based on the local maximum-entropy meshfree approximants [26]. These meshfree approximants are:

- C^∞, and therefore handle without difficulties the high-order character of the functionals,
- non-negative, and therefore possess monotonicity properties, as B-Splines and NURBS successfully applied to Cahn-Hilliard models [47],
- ideally suited for local refinement and dynamic adaptivity, as the basis functions rely only on the vicinity of neighboring nodes, instead of a mesh.

3. Ritz-Galerkin approximation of the functionals with maximum-entropy schemes

We describe here the numerical approximation of the variational problem to obtain equilibrium axisymmetric configurations for biomembranes. To fix the rigid body displacements of the membrane along the axis of symmetry, we need to supplement the P-F model given above with the constraint

$$M[\phi] = \int_\Omega \phi\,(z - z_c)\ d\Omega = 0,$$

where z_c allows us to center the phase-field solution in the simulation box.

We discretize the equations with local maximum-entropy approximation schemes. These meshfree approximants are non-negative and satisfy up to first-order consistency conditions. They have been shown to accurately approximate fourth-order PDE, such as the Kirchhoff-Love

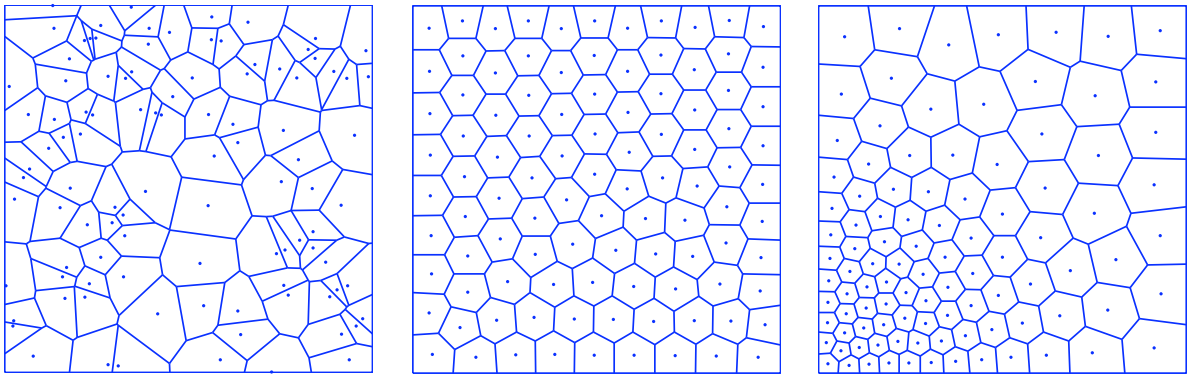

Figure 1: Voronoi tessellation for a random nodal distribution (left), CVT for a uniform density (center) and for a density function $\rho = 10 \exp\left[-2(x^2 + y^2)\right] + 0.1$ (right).

theory of thin shells [63, 64]. Second-order maximum entropy approximants have been developed [65, 66], and it has been shown that the linear approximants used here deliver comparable accuracy with a much simpler implementation. We follow a Ritz-Galerkin approach to approximate the variational formulation of the continuous problem by an algebraic optimization program, which we solve with an augmented Lagrangian method to impose the linear and nonlinear constraints, combined with L-BFGS and Newton-Rahpson nonlinear solvers. We locally adapt the node distribution to computationally afford very small values of ϵ by resorting to Centroidal Voronoi Tesselations (CVT) [67]. This method distributes nice grids of points obeying a prescribed density function, as illustrated in Figure 1. Here, we define the density functions such that the points are highly concentrated in the regions with high gradients of the phase-field (see Section 4.2).

3.1. Local maximum-entropy approximants

Meshfree methods define basis functions from a scattered set of nodes, not supported on a mesh as in traditional finite elements. The most popular meshfree approximants are based on the moving least squares (MLS) idea [68]. In recent years, the information theoretic concept of maximum-entropy has been put forth to develop polygonal approximants [69] and meshfree approximation schemes [26]. These maximum-entropy approximants present some advantages over MLS methods, such as their strict non-negativity, the straightforward imposition of boundary data, the robustness of their evaluation, or the simpler quadrature [65]. Moreover, the non-negativity and the linear reproducing conditions endow them with the structure of convex geometry [26], which enables the connection with other non-negative technologies like isogeometric analysis [46] or subdivision surfaces [70].

Maximum-entropy basis functions, denoted by $p_a(\boldsymbol{x}), a = 1, \ldots, N$ with $\boldsymbol{x} \in \mathbb{R}^d$, where d is the space dimension, are enforced to be non-negative and to fulfill the zeroth and first-order

consistency conditions

$$p_a(\boldsymbol{x}) \geq 0, \qquad \sum_{a=1}^{N} p_a(\boldsymbol{x}) = 1, \qquad \sum_{a=1}^{N} p_a(\boldsymbol{x})\ \boldsymbol{x}_a = \boldsymbol{x},$$

where the last equation allows us to identify the vectorial weights $\boldsymbol{x}_a$ with the positions of the nodes associated with each basis function.

The idea behind local maximum-entropy basis functions is to defined information-theoretical optimal approximants, only biased by locality, i.e. the property that the function approximation at a given point should depend on nodal values of nearby nodes. These approximants exhibit a (Pareto) compromise between two competing objectives, minimum width (locality) and entropy maximization (information theory optimality criteria), subject to the consistency constraints (reproducibility conditions). With these requirements, we write the following optimization program to select the approximants

$$\begin{aligned} \text{For fixed } \ \boldsymbol{x}, \ \text{minimize} \quad & \sum_{a=1}^{N} \beta_a p_a |\boldsymbol{x} - \boldsymbol{x}_a|^2 + \sum_{a=1}^{N} p_a \ln p_a \\ \text{subject to} \quad & p_a \geq 0, \quad a = 1, \dots, N \\ & \sum_{a=1}^{N} p_a = 1, \qquad \sum_{a=1}^{N} p_a \boldsymbol{x}_a = \boldsymbol{x}, \end{aligned}$$

where the non-negative nodal parameters $\beta_a = \gamma_a / h_a^2, \quad a = 1, \dots, N$ define the locality of the approximants [26, 71]. The dimensionless aspect ratio parameter γ_a characterizes the degree of locality of the basis function associated to the node $\boldsymbol{x}_a$, while h_a denotes a measure of the nodal spacing around node a. The local grid spacing h_a should be chosen to resolve the sharp features of the phase-field solutions, and should therefore be commensurate to ϵ. The basis functions become sharper and more local as the value of the dimensionless parameter γ_a increases, and the Delaunay approximants arise as specialized limits ($\gamma_a \geq 4$ in the practice), as illustrated in Figure 2 for a one-dimensional domain. In previous works, we characterized the behaviour of the approximants for problems involving higher-order derivatives, specifically for plates and thin-shells analysis [63, 66]. Typically, low values of γ_a lead to more accurate results for problems with smooth solutions, but also result in significantly more expensive calculations. This is due to the wider band-width and to the fact that more quadrature points are typically required. We found that the appropriate locality parameters are in the range $0.6 \leq \gamma \leq 1$, being $\gamma = 0.8$ the most convenient because it provides a good trade-off between computational cost and accuracy.

As detailed in [26], the optimization problem is smooth and convex, and admits a unique solution. An efficient solution follows from standard duality methods. Here, we just summarize the recipe for the calculation of the basis functions. By analogy with statistical mechanics, we define the partition function

$$Z(\boldsymbol{x}, \boldsymbol{\lambda}) = \sum_{b=1}^{N} \exp\left[-\beta_b |\boldsymbol{x} - \boldsymbol{x}_b|^2 + \boldsymbol{\lambda} \cdot (\boldsymbol{x} - \boldsymbol{x}_b)\right].$$

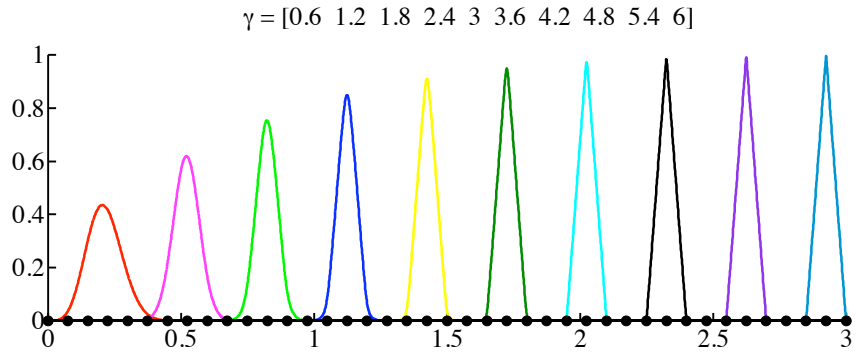

Figure 2: Seamless and smooth transition from meshfree to Delaunay affine basis functions. The transition is controlled by the non-dimensional nodal parameters γ_a, which here take linearly varying values from 0.6 (left) to 6 (right).

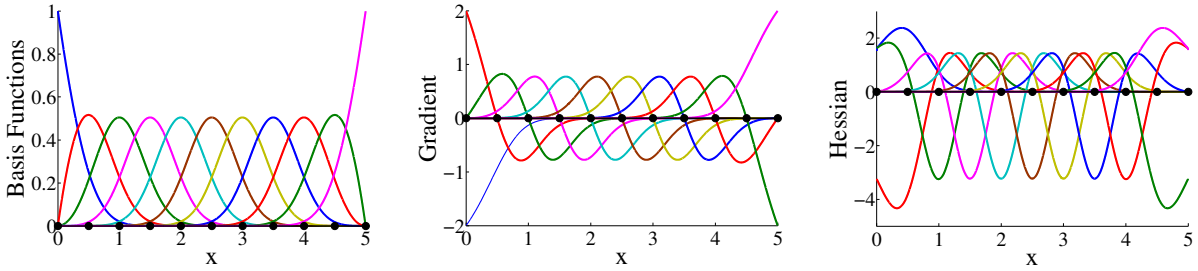

Figure 3: One-dimensional local maximum-entropy basis functions (left), and its first and second spatial derivatives (center-right) computed with a dimensionless parameter $\gamma = 0.8$.

At each evaluation point $\boldsymbol{x}$, the Lagrange multiplier for the linear consistency condition is the unique solution to a solvable, convex, unconstrained optimization problem

$$\boldsymbol{\lambda}^*(\boldsymbol{x}) = \arg\min_{\boldsymbol{\lambda}\in\mathbb{R}^d} \ln Z(\boldsymbol{x},\boldsymbol{\lambda}).$$

This optimization problem with d unknowns is efficiently solved with Newton's method. Then, the basis functions adopt the form

$$p_a(\boldsymbol{x}) = \frac{1}{Z\left(\boldsymbol{x},\boldsymbol{\lambda}^*(\boldsymbol{x})\right)} \exp\left[-\beta_a|\boldsymbol{x}-\boldsymbol{x}_a|^2 + \boldsymbol{\lambda}^*(\boldsymbol{x})\cdot(\boldsymbol{x}-\boldsymbol{x}_a)\right].$$

We refer to [64, 71] for the expressions to compute the gradient $\nabla p_a(\boldsymbol{x})$ and the Hessian matrix $Hp_a(\boldsymbol{x})$ of the local maximum-entropy basis functions, which are illustrated in Figure 3 for a one-dimensional domain uniformly discretized and a dimensionless parameter $\gamma = 0.8$.

Some properties of the local maximum-entropy approximants, such as smoothnes and variation diminishing properties [26], are illustrated in Figure 4. These approximants also satisfy *ab initio* a weak Kronecker-delta property at the boundary of the convex hull of the nodes [26]. With this property, the imposition of essential boundary conditions in Galerkin methods

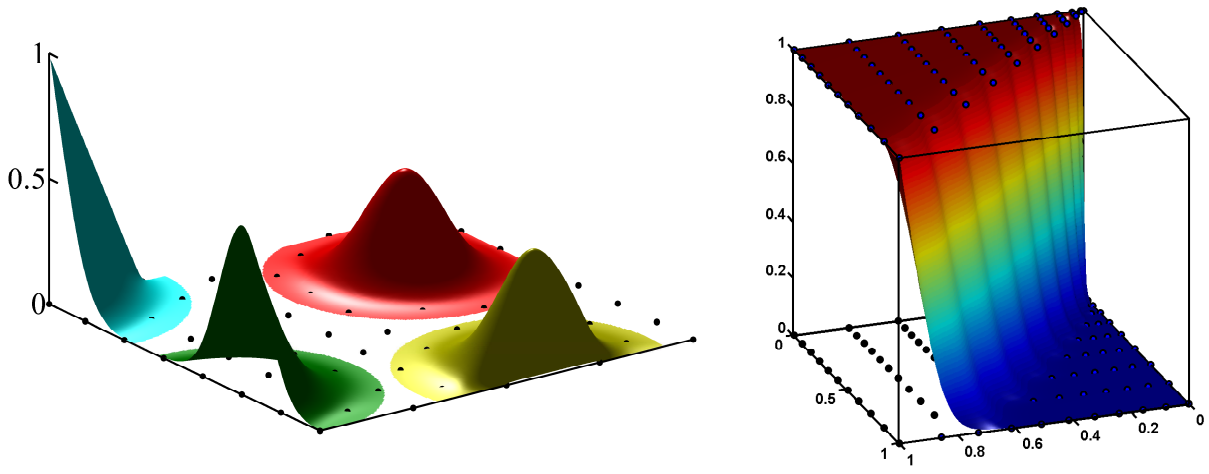

Figure 4: Illustration of non-negativity, smoothness and weak Kronecker-delta properties for two-dimensional local maximum-entropy basis functions (left), and the variation diminishing property (right).

is straightforward. Moreover, the approximants are multidimensional and lead to well behaved mass matrices [26]. We refer to [66] for a more detailed description of maximum-entropy approximants and their applications.

3.2. Discretization of the minimization problem

We consider the following expansion for the phase-field in terms of the basis functions

$$\phi(\boldsymbol{x}) \approx \phi_h(\boldsymbol{x}, \boldsymbol{\Phi}) = \sum_{a=1}^{N} p_a(\boldsymbol{x})\phi_a,$$

where $\boldsymbol{\Phi} = (\phi_1, \phi_2, ..., \phi_N)$ is an array containing the N nodal values of the phase-field, and insert this ansatz into the variational problem describing the P-F model to obtain the following algebraic optimization program:

$$\begin{aligned}
\text{Minimize} \quad & E_h(\boldsymbol{\Phi}) = E[\phi_h] = f_E \frac{k}{2\epsilon} \int_\Omega W_h^2 \, d\Omega \\
\text{subject to} \quad & V_h(\boldsymbol{\Phi}) = V[\phi_h] = \frac{1}{2}\left(Vol(\Omega) + \int_\Omega \phi_h \, d\Omega \right) = V_0 \\
& A_h(\boldsymbol{\Phi}) = A[\phi_h] = f_A \int_\Omega \left[\frac{\epsilon}{2} |\nabla \phi_h|^2 + \frac{1}{4\epsilon}(\phi_h^2 - 1)^2 \right] \, d\Omega = A_0 \\
& M_h(\boldsymbol{\Phi}) = M[\phi_h] = \int_\Omega \phi_h (z - z_c) \, d\Omega = 0 \\
& \phi_h|_{\partial\Omega} = -1,
\end{aligned} \tag{1}$$

where

$$W_h = \epsilon \Delta \phi_h + \left(\frac{1}{\epsilon}\phi_h + C_0\sqrt{2} \right)\left(1 - \phi_h^2\right).$$

The optimality conditions can be obtained from differentiating the Lagrangian function

$$\mathcal{L}(\boldsymbol{\Phi}, \boldsymbol{\nu}) = E_h(\boldsymbol{\Phi}) - \nu_A \left[A_h(\boldsymbol{\Phi}) - A_0\right] - \nu_V \left[V_h(\boldsymbol{\Phi}) - V_0\right] - \nu_M \left[M_h(\boldsymbol{\Phi}) - M_0\right],$$

where the area, volume and static moment constraints are maintained by the Lagrange multipliers $\boldsymbol{\nu} = (\nu_A, \nu_V, \nu_M)$. Physically, ν_A is a membrane tension and ν_V a pressure difference between the inside and the outside of the vesicle.

After defining a new set of variables $(\boldsymbol{\Phi}, \boldsymbol{\nu}) = (\phi_1, \phi_2, ..., \phi_N, \nu_A, \nu_V, \nu_M)$, the optimal solution of this saddle-point problem can be sought with the Newton-Raphson method applied to the nonlinear system of equations $\partial_{\boldsymbol{\Phi}}\mathcal{L} = 0$, $\partial_{\boldsymbol{\nu}}\mathcal{L} = 0$. However, this approach may lead to mere stationary points, not minimizers of the elastic energy (physically unstable equilibria). Furthermore, given the difficulty in setting good initial guesses for the Lagrange multipliers, this solution strategy is not robust.

A robust strategy that guarantees stable equilibria is based on the augmented Lagrangian method, which combines the standard Lagrangian with penalties. This method retains the exactness of the Lagrange multipliers method and the minimization principle of penalty methods. The minimization is performed iteratively on the phase-field variables only for frozen Lagrange multipliers, which are updated explicitly (see [72, 73] for further details). The augmented Lagrangian is

$$\begin{aligned}\mathcal{L}_A(\boldsymbol{\Phi}, \boldsymbol{\nu}) = E_h(\boldsymbol{\Phi}) &- \nu_A \left[A_h(\boldsymbol{\Phi}) - A_0\right] - \nu_V \left[V_h(\boldsymbol{\Phi}) - V_0\right] - \nu_M \left[M_h(\boldsymbol{\Phi}) - M_0\right] \\ &+ \frac{1}{2\mu} \left|A_h(\boldsymbol{\Phi}) - A_0\right|^2 + \frac{1}{2\mu} \left|V_h(\boldsymbol{\Phi}) - V_0\right|^2 + \frac{1}{2\mu} \left|M_h(\boldsymbol{\Phi}) - M_0\right|^2.\end{aligned}$$

We solve the problem in two stages. First, we follow the augmented Lagrangian method to find an approximate minimizer consistent with the constraints with a coarse tolerance. Then, this approximation is refined with the regular Newton-Raphson method on the extended set of variables $(\boldsymbol{\Phi}, \boldsymbol{\nu})$. Since the initial guess for this second stage is very close to a minimizer, the algorithm never leads to unstable equilibria. The expressions to compute the gradients $\tilde{\boldsymbol{r}}(\boldsymbol{\Phi}, \boldsymbol{\nu})$ and $\tilde{\boldsymbol{r}}_A(\boldsymbol{\Phi}, \boldsymbol{\nu})$, as well as the hessians, of the Lagrangian and augmented Lagrangian, respectively, are given in Appendix A.

All the integrals in Eq. (1) and in its variations, see Appendix A, are approximated with numerical quadrature based on a background integration grid, as usually done in Galerkin meshfree methods (see [26] and references therein). Here, we consider Gaussian quadrature rules supported on the Delaunay triangulation associated with the set of nodes, although other specialized techniques are available [74].

4. Numerical Examples

The phase diagram for the equilibrium shapes of vesicles has been extensively studied (see [4, 75] and references therein). This diagram exhibits a number of equilibrium branches, including prolates, oblates, discocytes, or stomatocytes. The equilibrium shape for a given area, volume, and spontaneous curvature is not unique in general. For instance, upon deflation of an initially spherical vesicle without spontaneous curvature, the prolate-dumbbell and oblate-discocyte branches are possible, as illustrated in Figure 5. Mathematically, the shape transitions

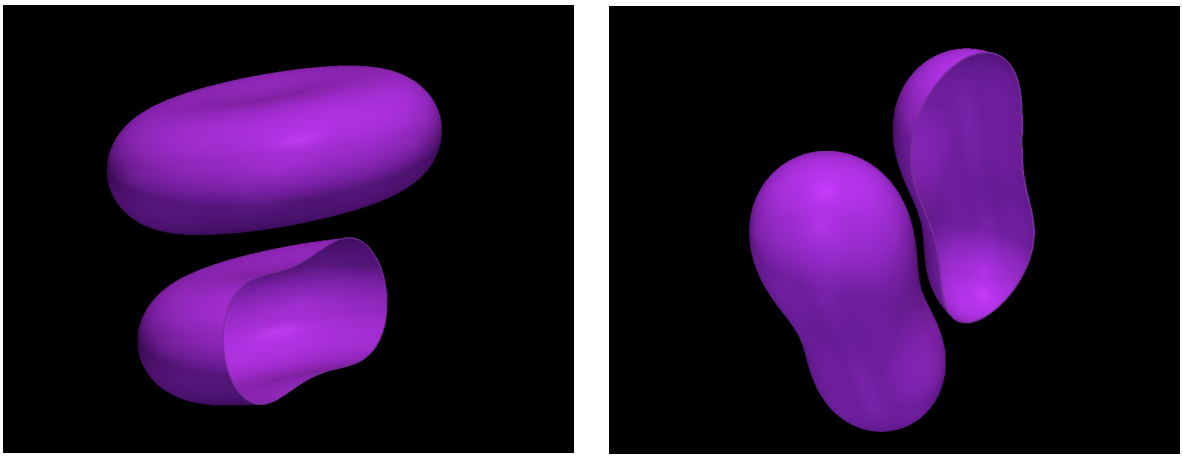

Figure 5: 3D view of discocyte (left) and dumbbell (right) equilibrium shapes.

and the equilibrium branches can be tracked by changing the volume constraint and solving for constrained minimizers. A number of equilibrium shapes for the oblate equilibrium branch are plotted in Figure 6. Each shape is an energy minimizer with fixed area and volume, after reducing by 5% the volume of the previous configuration. The computations are carried out with a uniform grid and a regularization parameter $\epsilon = 0.02$. In all the calculations, we take $C_0 = 0$ and $S_0 = 4\pi R^2$, with $R = 0.4$. The relative error in the energy is approximately 2% as compared to the sharp interface approach.

The accuracy of phase-field solutions relative to the sharp interface model is intrinsically linked to the regularization parameter ϵ, which in turn sets bounds on the required resolution of the computational grid. This motivates us to study two relevant aspects of the proposed approach: (i) the convergence as the number of points increases for a fixed regularization parameter ϵ and uniform grid, and (ii) the convergence to a sharp model as regularization parameter is decreased ($\epsilon \to 0$) and the grid of points is adapted.

To answer these questions, we analyze two specific equilibrium shapes, a discocyte and a dumbbell configuration, both of them with spontaneous curvature $C_0 = 0$. For the S-I model and the sphere, we have $A_{sphere} = 4\pi R^2 = 0.64\pi$, $V_{sphere} = \frac{4}{3}\pi R^3 \approx 0.08533\pi$ and $E_{sphere} = 2\pi$. The discocyte and dumbbell configurations are found by minimization of the curvature energy with constraints $A_0 = A_{sphere} = 0.64\pi$ and $V_0 = 0.8\ V_{sphere} \approx 0.06826\pi$, i.e. the volume of the sphere is reduced by 20%. The energies of the sharp interface model for the discocyte and dumbbell equilibrium shapes are $E_{discocyte} = 9.12657$ and $E_{dumbbell} = 8.71756$. These energies are computed with an overkill B-spline discretization of the S-I Model.

4.1. Convergence for fixed regularization parameter ϵ and uniform grids of points

Table 1 shows the numerical energies for the discocyte equilibrium shape considering different values of ϵ and several grids of points in a computational domain $\Omega = [0, 1.5] \times [0, 2]$. The identification code (O for the oblate-discocyte branch, P for the prolate-dumbbell branch) and the number of nodes for each grid are indicated in the first and the second column. As the grids

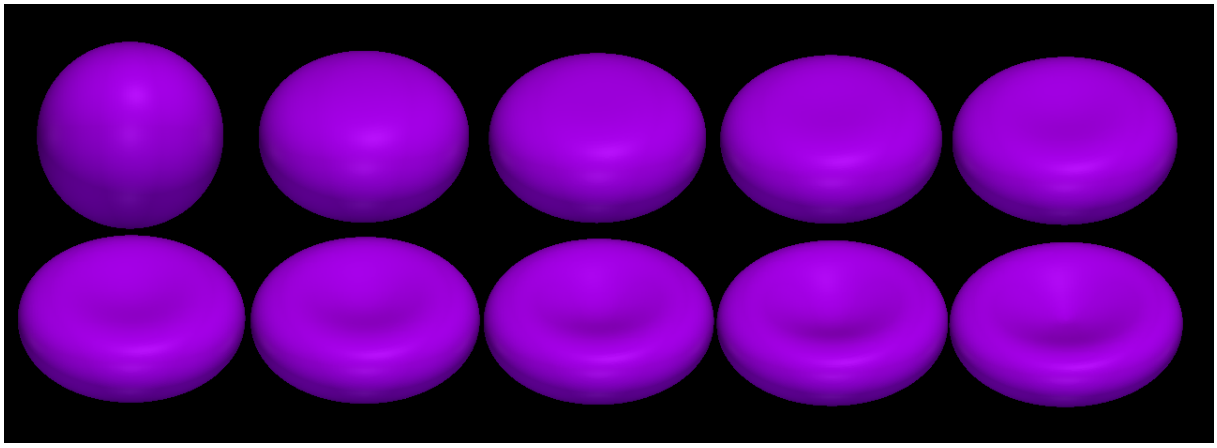

Figure 6: 3D views of the oblate equilibrium branch: each shape is computed by minimizing the energy and reducing by 5% the volume of the previous configuration.

Table 1: Energies of the discocyte equilibrium shape for different uniform grids of points and several values of ϵ. The size of the computational domain is $\Omega = [0, 1.5] \times [0, 2]$. Reference energy from a sharp interface simulation: $E_{discocyte} = 9.12657$.

ID	# nodes	$\bar{h}$	$\epsilon = 0.05$	$\epsilon = 0.04$	$\epsilon = 0.03$	$\epsilon = 0.02$	$\epsilon = 0.01$
O1	6124	0.024	9.71279	9.59056	–	–	–
O2	12271	0.017	9.72137	9.59446	9.43775	–	–
O3	24597	0.012	9.72671	9.59553	9.43483	9.29532	–
O4	49145	0.0084	9.73203	9.59786	9.43515	9.28938	–
O5	98388	0.0059	9.73536	9.59901	9.43481	9.28674	9.22082
O6	146545	0.0048	9.73716	9.59948	9.43422	9.28378	9.19139
O7	296344	0.0034	9.73989	9.60053	9.43437	9.28326	9.18627

Table 2: Energies of the dumbbell equilibrium shape for different uniform grids of points and several values of ϵ. Reference energy from a sharp interface simulation: $E_{dumbbell} = 8.71756$.

ID	# nodes	$\bar{h}$	$\epsilon = 0.05$	$\epsilon = 0.04$	$\epsilon = 0.03$	$\epsilon = 0.02$	$\epsilon = 0.01$
P1	6124	0.024	9.29504	9.15560	–	–	–
P2	12271	0.017	9.30167	9.15918	9.00361	–	–
P3	24597	0.012	9.30627	9.16106	9.00310	8.87045	–
P4	49145	0.0084	9.31053	9.16315	9.00362	8.86669	–
P5	98388	0.0059	9.31307	9.16407	9.00331	8.86445	8.81432
P6	146545	0.0048	9.31439	9.16421	9.00217	8.86005	8.77677
P7	296344	0.0034	9.31650	9.16512	9.00251	8.86033	8.77359

are not perfectly uniform (see Figure 7, for instance), the value of the average nodal spacing $\bar{h}$ is reported in the third column. The remaining columns show the energies computed for different values of the regularization parameter ϵ. We report the energies only when the transition profile is reasonably resolved, as decided by the relation $\epsilon > 2h$. Note the energy convergence from above as the number of points increases for each ϵ (columns). We can also observe how the value of the energy converges to the sharp interface value $E_{discocyte} = 9.12657$ as the parameter ϵ decreases.

In experiments not reported here, we consider the same problem in a slightly smaller domain $\Omega_1 = [0, 1]\times[0, 2]$. We find that for the larger values ϵ, the phase-field interacts with the boundary of the simulation box, resulting in higher energies. The influence of the domain size on the results further highlights the need for adaptivity, as local refinement makes it computationally affordable to increase significantly the size of the simulation box.

Table 2 reports the numerical energies for the dumbbell shape considering different values of ϵ and several refinements of the grid of points. We observe that the convergence both for ϵ and $\bar{h}$ presents the same behavior described for the discocyte shape.

4.2. Convergence as $\epsilon \to 0$ and adapted grids of points

As argued earlier, adaptivity is essential for numerical approaches based on phase-field models to be competitive. We now describe the node density function considered here to relocate the nodes following the CVT method. The phase-field is constant in a large part of the domain and presents a sharp variation in the thin region corresponding to the smeared interface. To capture this behavior, consider the density function

$$\rho(\boldsymbol{x}) = 1 + f\ |\nabla\phi(\boldsymbol{x})|$$

where f is an amplification factor. This heuristic density function allows us to obtain a uniform nodal distribution where the phase-field is constant, since $|\nabla\phi(\boldsymbol{x})| = 0$, and to locally concentrate in zones where the field changes abruptly. The factor f gives us the flexibility to increase/decrease the weight of the gradient, which in turn increases/decreases the local concentration of nodes.

A possible strategy for adaptivity is to solve the optimization problem with a coarse grid of points (and thus a large value of ϵ), apply CVT to redistribute the nodes concentrating them

Table 3: Energies of the discocyte equilibrium shape for several values of ϵ and uniform and adapted grids of 6,124 points. See Table B.6 for a description of the grids of points. Reference energy from a sharp interface simulation: $E_{discocyte} = 9.12657$.

ID	# nodes	$\epsilon = 0.04$	$\epsilon = 0.03$	$\epsilon = 0.025$	$\epsilon = 0.02$	$\epsilon = 0.015$	$\epsilon = 0.01$
O1	6124	9.59056	–	–	–	–	–
O11	6124	9.59678	9.44002	–	–	–	–
O12	6124	–	9.43506	9.35810	9.28849	–	–
O13	6124	–	–	9.35970	9.28701	9.22588	9.18703
O7	296344	9.60053	9.43437	9.35488	9.28326	9.22399	9.18627

around the interface, and compute the phase-field solution with a smaller ϵ for this new distribution of points. In practice, this strategy cannot be applied at once with a large amplification factor f. Indeed, the initial coarse grid provides an inaccurate phase-field solution, which in turn produces an inadequate relocation of the points. This ultimately constraints unphysically the phase-field solutions. A better strategy is to adapt the grid and reduce ϵ progressively, with moderate values of f.

Table 3 reports the bending energies of the discocyte equilibrium shape for uniform and adapted grids and several regularization parameters. The first and the last rows correspond to uniform meshes with 6,124 and 296,344 nodes, and are the same as those reported in Table 1. The other rows correspond to adapted grids with 6,124 nodes, obtained in each step of the progressive adaption of the grid and reduction of ϵ. The first column of the table gives an identification code for the grids of points. A description of the features of each grid is given in Table B.6, and some of the grids are shown in Figure 7. The smooth transition between the successive grids is apparent in the figure, as the value of ϵ is slowly decreased in each step, while f is increased to maintain the relative effect of the phase-field gradient. The minimum allowable value for the regularization parameter ϵ_{min} for a given grid is determined by the nodal spacing distribution, as detailed in Appendix B. As expected, the ability of adapted grids to accurately support sharp phase-field solutions at an affordable cost is noteworthy. Adapted grids grant the same accuracy (measured by the optimal energy) as uniform grids with a 50-fold reduction in the number of degrees of freedom for $\epsilon = 0.01$.

Figure 7 (bottom) shows the equilibrium phase-field for the grids referred to in Table 3 and shown in Figure 7 (top, center). It can be noticed that as the value of ϵ decreases, the thickness of the diffuse interface shrinks considerably. Figure 8 (a) illustrates the phase-field solution computed with grid O13 and $\epsilon = 0.01$; an abrupt transition can be observed between the inner ($\phi_h = 1$) and the outer ($\phi_h = -1$) regions. The superposition of the sharp interface solution with the zero phase-field level set ($\phi_h = 0$) is shown in Figure 8 (b). The two curves nearly lie on top of each other, illustrating numerically the connection between the phase-field and the sharp interface models.

Figure 8(c-e) shows cross sections of the phase-field solutions depicted in Figure 7 (bottom). The position of the cross section is indicated in Figure 8 (b) with a dashed-dotted cutline. The cross section corresponding to $\epsilon = 0.005$ is computed with an adapted grid of 24,597 nodes, as explained later. This figure highlights how the variation dimishing property (informally, the approximation is not more wiggly than the data) of the local, smooth, non-negative maximum-

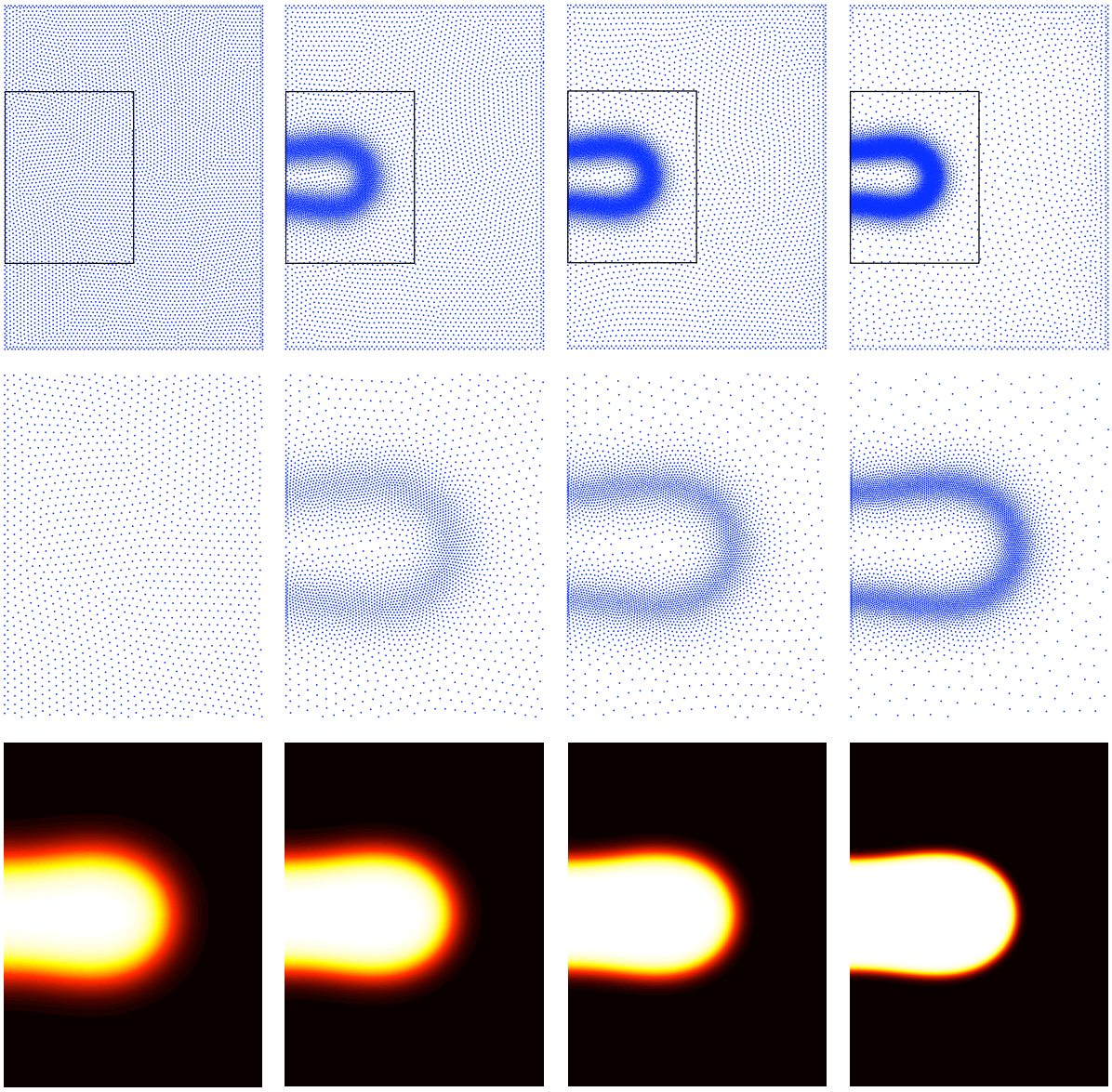

Figure 7: Discocyte equilibrium shape. Uniform and adapted grids of 6,124 points (top). From left to rigth: O1, O11, O12 and O13. Zoom of the areas indicated with black boxes (center). Phase-field (bottom). From left to rigth, the solutions correspond to $\epsilon = 0.04$, $\epsilon = 0.03$, $\epsilon = 0.02$, and $\epsilon = 0.01$. The values of energy for each solution are given in Table 3.

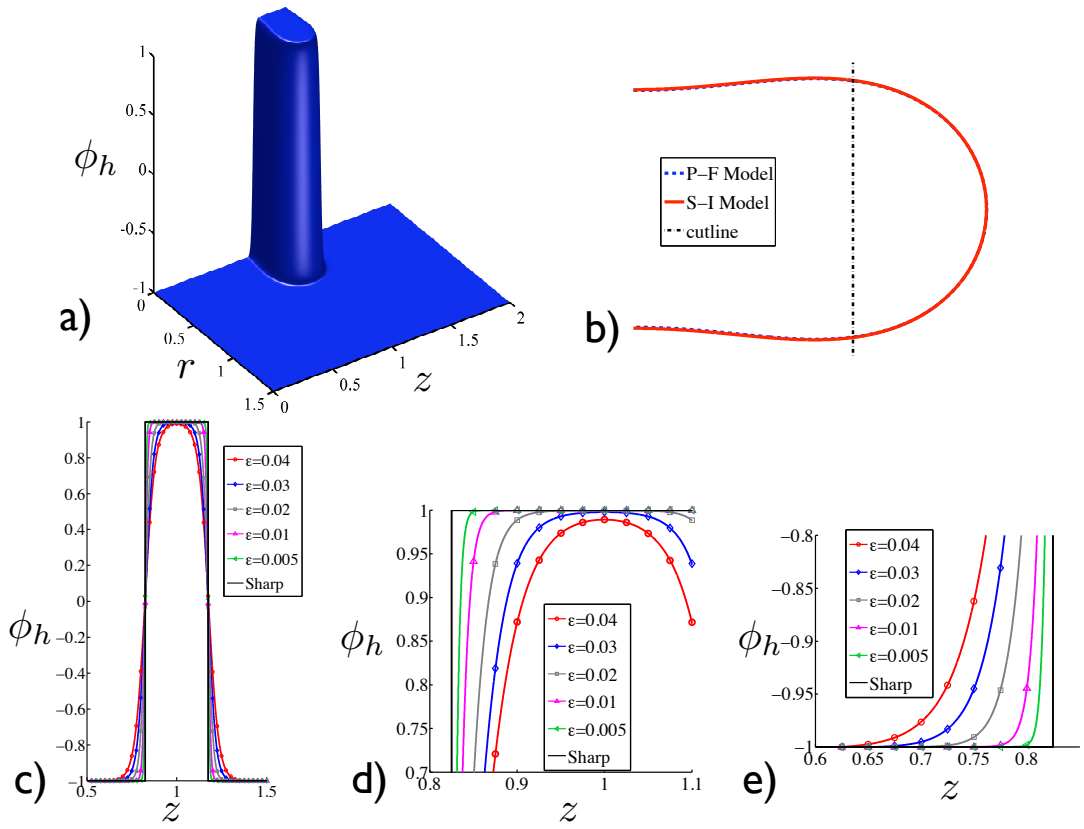

Figure 8: Phase-field solution for the discocyte equilibrium shape: (a) abrupt transition between inner ($\phi_h = 1$) and outer ($\phi_h = -1$) regions, and (b) superposition of the sharp interface solution and zero phase-field level set $\phi_h = 0$. The phase-field solution is obtained with an adapted grid of 6,124 nodes and $\epsilon = 0.01$. (c) Cross sections corresponding to the cutline indicated in (b) of the phase-field solutions with different values of ϵ. This plot, together with the zooms in (d) and (e), illustrates the absence of oscillations or overshoots near the interface, and how the interfacial thickness decreases as ϵ is reduced. The sharp interface solution is shown for comparison.

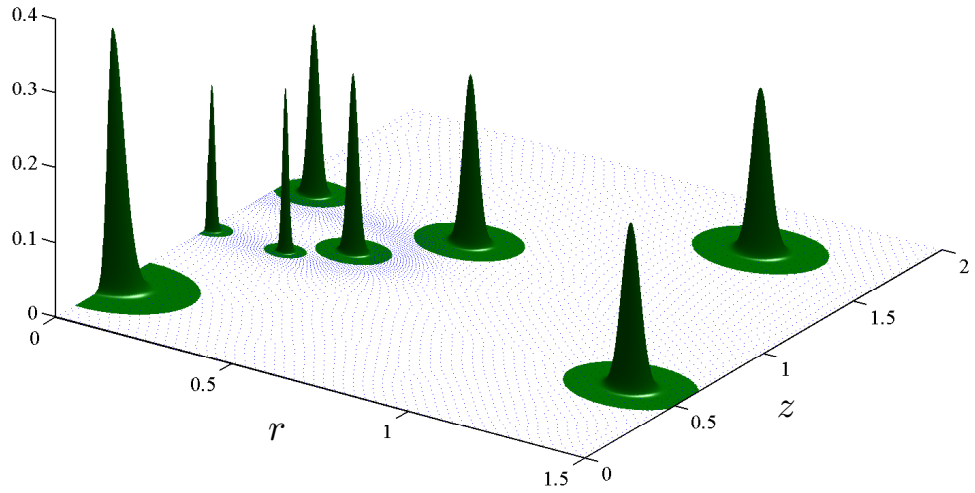

Figure 9: Illustration of the uniform aspect ratio of the basis functions, despite the strong non-uniformity of the nodal spacing (discocyte solution, N=6,124, grid O13).

Table 4: Relative error (%) measured in energy for the discocyte equilibrium shape and several values of the regularization parameter ϵ and different uniform (Un) and adapted (Ad) grids. The energy of the shape-interface model $E_{discocyte} = 9.12657$ is used as reference.

# nodes	Grid	$\epsilon = 0.03$	$\epsilon = 0.025$	$\epsilon = 0.02$	$\epsilon = 0.015$	$\epsilon = 0.01$	$\epsilon = 0.007$	$\epsilon = 0.005$
6124	Ad	3.38	2.55	1.76	1.09	0.66	–	–
12271	Ad	3.34	2.49	1.69	1.11	0.62	0.57	–
24597	Ad	3.37	2.51	1.69	1.12	0.63	–	0.43
296344	Un	3.37	2.50	1.72	1.07	0.65	–	–

entropy approximants results in monotone solutions of the phase-field PDE, devoid of spurious oscillations even for very sharp transitions. A selection of the basis functions for grid O13 are shown in Figure 9. The uniform aspect ratio of the interior basis functions is noteworthy, despite the strong non-uniformity of the grid. The monotonicity of the approximants does not immediately imply that the numerical solutions of the phase-field PDE is free of overshoots outside of the physically meaningful limits $-1 \leq \phi \leq 1$, but the numerical evidence suggests that this is the case. Further numerical analysis is required to clarify this issue. Again, the convergence of the phase-field solutions to the sharp interface stepped solution as $\epsilon \to 0$ is apparent. Similar conclusions were drawn from isogeometric simulations of the Cahn-Hilliard and isothermal Navier-Stokes-Korteweg phase-field equations, where similar smooth non-negative basis functions, albeit structured in nature, were used [47, 48].

We repeat the refinement experiments reported in Table 3 with grids of 12,271 and 24,597 nodes. The larger number of nodes allows us to resolve the phase-field model with $\epsilon = 0.007$ for the grid of 12,271 points, yielding $E_{\epsilon=0.007} = 9.17824$, and with $\epsilon = 0.005$ for the grid of 24,597 points, yielding $E_{\epsilon=0.005} = 9.16539$. Table 4 shows the relative errors in energy between the sharp interface solution and the the adapted phase-field solutions for different number of nodes

Table 5: Energies of the dumbbell equilibrium shape for several values of ϵ and uniform and adapted grids of 6,124 points. See Table B.6 for a description of the grids. Reference energy from a sharp interface simulation: $E_{dumbbell} = 8.71756$.

ID	# nodes	$\epsilon = 0.04$	$\epsilon = 0.03$	$\epsilon = 0.025$	$\epsilon = 0.02$	$\epsilon = 0.015$	$\epsilon = 0.01$
P1	6124	9.15559	–	–	–	–	–
P11	6124	9.16513	9.01027	8.93545	–	–	–
P12	6124	–	9.00358	8.92990	8.86381	8.80003	–
P13	6124	–	–	8.92452	8.86090	8.80834	8.77909
P7	296344	9.16512	9.00251	8.92706	8.86033	8.80628	8.77359

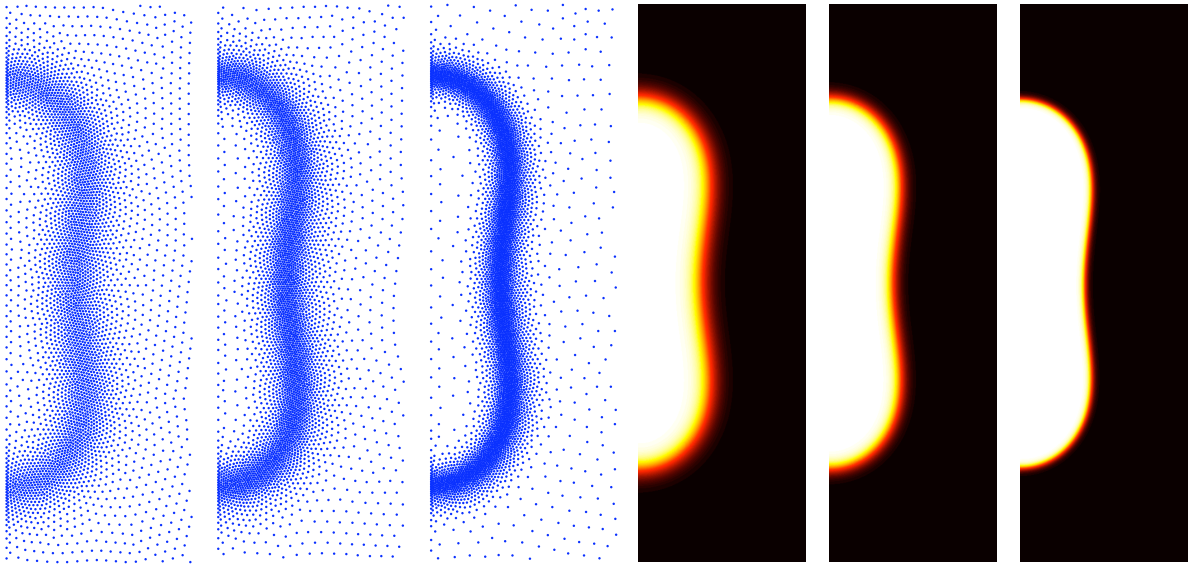

Figure 10: Distribution of points and phase-field density for adapted grids of 6,124 nodes (dumbbell equilibrium shape). The values of energy for each solution are indicated in the Table 5.

and several values of ϵ. It can noticed that, with our criterion to select ϵ_{min} for a given grid, the adapted grids resolve the width of the smeared interface, and the error depends basically on ϵ. Again, it is clear that the adaptive strategy can deliver very accurate solutions (error in the energy below 0.5%) for very small values of the regularization parameter ϵ with a reduced number of degrees of freedom.

We repeat the experiments for a dumbbell equilibrium shape. We observe the same behavior as reported in Table 5. Figure 10 illustrates adapted grids of 6,124 points with the corresponding phase-field solution for the regularization parameters $\epsilon = 0.03$, $\epsilon = 0.02$ and $\epsilon = 0.01$.

5. Conclusions

We have proposed an adaptive meshfree Ritz-Galerkin method to numerically approximate phase-field models of biomembranes. We have shown the ability of the proposed method, based

on local smooth non-negative approximants, to deal directly with the high-order character of the equations. Furthermore, adaptivity is very natural for a meshfree method, and proves essential to resolve the sharp features of the phase-field model at an affordable cost. We have shown that the adaptive method is able to resolve phase-field models with very small regularization parameter and numerically converge to the sharp interface limit. The method proposed here combines the adaptive capabilities of C^0 finite elements, which nevertheless require reformulating the fourth-order PDE as a system of second-order PDEs, hence introducing extra degrees of freedom, with the simplicity of tensor product methods, which do not require reformulations of the model.

An important issue in the adaptive strategy is to avoid excessive variations of the nodal spacing. Otherwise, the resulting meshfree basis functions can exhibit irregular features, which are difficult to integrate. CVT provides us with high quality graded distributions of points by designing an appropriate heuristic density function, although it can be computationally expensive. However, as discussed in a companion paper [27], in the proposed Lagrangian method for the dynamics of biomembranes in a viscous fluid, the CVT grid and its associated quadrature points and weights must only be computed once at the beginning of the calculation, and has a negligible cost overall. Furthermore, the strategy to adapt the nodes is not essential to the proposed method and other algorithms, such as octree methods, are more suitable and efficient to locally refine grids in 3D.

The calculations presented here are not practical in many situations of interest to assess the mechanics of vesicles and biomembranes in general, as these display very large and sometimes abrupt shape changes as the control parameters are changed. Locally refined grids impose very serious biases on the resolvable solutions, particularly when in a given optimization step, the system buckles to a distant equilibrium shape. In a companion paper [27] we present a Lagrangian method to deal with the coupled fluid-membrane overdamped dynamics, which exploits the virtues of the method presented here as the local refinement follows naturally with the Lagrangian flow the sharp features of the phase-field. This combination of methods shows promise for robust, scalable computations of complex membrane systems in three dimensions.

Acknowledgments

We acknowledge the support of the European Research Council under the European Community's 7th Framework Programme (FP7/2007-2013)/ERC grant agreement nr 240487, and of the Ministerio de Ciencia e Innovación (DPI2011-26589). MA acknowledges the support received through the prize "ICREA Academia" for excellence in research, funded by the Generalitat de Catalunya. CP acknowledges FPI-UPC Grant, FPU Ph. D. Grant (Ministry of Science and. Innovation, Spain) and Col·legi d'Enginyers de Camins, Canals i Ports de Catalunya for their support.

Appendix A. Derivatives for the optimization problem

In Section 3.2 we introduce a discretization for the continuum phase-field

$$\phi(\boldsymbol{x}) \approx \phi_h(\boldsymbol{x}, \boldsymbol{\Phi}) = \sum_{a=1}^{N} p_a(\boldsymbol{x})\phi_a,$$

where $p_a(\boldsymbol{x})$ denote the meshfree maximum-entropy approximants and $\boldsymbol{\Phi} = (\phi_1, \phi_2, ..., \phi_N)$ the array containing the N nodal values of the phase-field. The gradient and the hessian of the phase-field follow as

$$\nabla\phi(\boldsymbol{x}) \approx \nabla\phi_h(\boldsymbol{x}, \boldsymbol{\Phi}) = \sum_{a=1}^{N} \nabla p_a(\boldsymbol{x})\phi_a \quad \text{and} \quad H\phi(\boldsymbol{x}) \approx H\phi_h(\boldsymbol{x}, \boldsymbol{\Phi}) = \sum_{a=1}^{N} Hp_a(\boldsymbol{x})\phi_a.$$

The problem posed in Eq. (1) also requires the calculation of the Laplacian of the phase-field, whose expression in Cartesian coordinates is $\Delta\phi(\boldsymbol{x}) \approx \Delta\phi_h(\boldsymbol{x}) = \text{tr}\left[H\phi_h(\boldsymbol{x}, \boldsymbol{\Phi})\right]$. As we consider axisymmetric solutions, we use cylindrical coordinates, which result in

$$\Delta\phi(\boldsymbol{x}) \approx \Delta\phi_h(\boldsymbol{x}, \boldsymbol{\Phi}) = \frac{1}{r}\frac{\partial\phi_h}{\partial r} + \frac{\partial^2\phi_h}{\partial r^2} + \frac{\partial^2\phi_h}{\partial z^2}.$$

To compute the gradient of the Lagrangian and the augmented Lagrangian, we need the derivatives of E_h, V_h, A_h and M_h with respect to the nodal values $\boldsymbol{\Phi}$

$$\begin{aligned}
\left[\partial_{\boldsymbol{\Phi}} E_h\right]_a &= \frac{\partial E_h}{\partial \phi_a} = \ f_E \frac{k}{2\epsilon}\int_\Omega 2W_h \frac{\partial W_h}{\partial \phi_a}\ d\Omega, \\
\left[\partial_{\boldsymbol{\Phi}} V_h\right]_a &= \frac{\partial V_h}{\partial \phi_a} = \ \frac{1}{2}\int_\Omega p_a\ d\Omega, \\
\left[\partial_{\boldsymbol{\Phi}} A_h\right]_a &= \frac{\partial A_h}{\partial \phi_a} = \ f_A \int_\Omega \left[\epsilon\nabla\phi_h\cdot\nabla p_a + \frac{1}{\epsilon}p_a\phi_h(\phi_h^2 - 1)\right]\ d\Omega, \\
\left[\partial_{\boldsymbol{\Phi}} M_h\right]_a &= \frac{\partial M_h}{\partial \phi_a} = \ \int_\Omega p_a(z - z_c)\ d\Omega,
\end{aligned}$$

where

$$W_h = \epsilon\Delta\phi_h + \left(\frac{1}{\epsilon}\phi_h + C_0\sqrt{2}\right)\left(1 - \phi_h^2\right),$$

$$\frac{\partial W_h}{\partial \phi_a} = \epsilon\frac{\partial\Delta\phi_h}{\partial\phi_a} + \frac{p_a}{\epsilon} - p_a\phi_h\left(\frac{3}{\epsilon}\phi_h + 2C_0\sqrt{2}\right),$$

and

$$\frac{\partial\Delta\phi_h}{\partial\phi_a} = \frac{1}{r}\frac{\partial p_a}{\partial r} + \frac{\partial^2 p_a}{\partial r^2} + \frac{\partial^2 p_a}{\partial z^2}.$$

The calculation of the hessian of the Lagrangian and the augmented Lagrangian also requires the second derivatives of E_h, V_h, A_h and M_h with respect to $\boldsymbol{\Phi}$

$$\begin{aligned}
\left[\partial_{\boldsymbol{\Phi}}\partial_{\boldsymbol{\Phi}} E_h\right]_{ab} &= \frac{\partial^2 E_h}{\partial\phi_a\partial\phi_b} = f_E\frac{k}{2\epsilon}\int_\Omega 2\left(\frac{\partial W_h}{\partial\phi_a}\frac{\partial W_h}{\partial\phi_b} + W_h\frac{\partial^2 W_h}{\partial\phi_a\partial\phi_b}\right)\ d\Omega, \\
\left[\partial_{\boldsymbol{\Phi}}\partial_{\boldsymbol{\Phi}} V_h\right]_{ab} &= \frac{\partial^2 V_h}{\partial\phi_a\partial\phi_b} = 0, \\
\left[\partial_{\boldsymbol{\Phi}}\partial_{\boldsymbol{\Phi}} A_h\right]_{ab} &= \frac{\partial^2 A_h}{\partial\phi_a\partial\phi_b} = f_A\int_\Omega\left[\epsilon\nabla p_a\cdot\nabla p_b + \frac{1}{\epsilon}p_a p_b(3\phi_h^2 - 1)\right]\ d\Omega, \\
\left[\partial_{\boldsymbol{\Phi}}\partial_{\boldsymbol{\Phi}} M_h\right]_{ab} &= \frac{\partial^2 M_h}{\partial\phi_a\partial\phi_b} = 0,
\end{aligned}$$

where

$$\frac{\partial^2 W_h}{\partial \phi_a \partial \phi_b} = -2 p_a p_b \left(\frac{3}{\epsilon} \phi_h + C_0 \sqrt{2} \right).$$

After defining a new set of variables $\tilde{\boldsymbol{x}} = (\boldsymbol{\Phi}, \boldsymbol{\nu}) = (\phi_1, \phi_2, ..., \phi_N, \nu_A, \nu_V, \nu_M)$, where $\boldsymbol{\nu}$ denotes the set of Lagrange multipliers, the gradient $\tilde{\boldsymbol{r}}(\tilde{\boldsymbol{x}})$ for the Lagrangian is given by

$$\tilde{\boldsymbol{r}}(\tilde{\boldsymbol{x}}) = \partial_{\tilde{\boldsymbol{x}}} \mathcal{L}(\tilde{\boldsymbol{x}}) = \left[\partial_{\boldsymbol{\Phi}} \mathcal{L}(\tilde{\boldsymbol{x}}) \; \partial_{\boldsymbol{\nu}} \mathcal{L}(\tilde{\boldsymbol{x}}) \right]^T,$$

where

$$\partial_{\boldsymbol{\Phi}} \mathcal{L}(\tilde{\boldsymbol{x}}) = \partial_{\boldsymbol{\Phi}} E_h(\boldsymbol{\Phi}) - \nu_A \partial_{\boldsymbol{\Phi}} A_h(\boldsymbol{\Phi}) - \nu_V \partial_{\boldsymbol{\Phi}} V_h(\boldsymbol{\Phi}) - \nu_M \partial_{\boldsymbol{\Phi}} M_h(\boldsymbol{\Phi}),$$

and

$$\partial_{\boldsymbol{\nu}} \mathcal{L}(\tilde{\boldsymbol{x}}) = \left[(A_h(\boldsymbol{\Phi}) - A_0) \;\; (V_h(\boldsymbol{\Phi}) - V_0) \;\; (M_h(\boldsymbol{\Phi}) - M_0) \right].$$

The hessian $\tilde{\boldsymbol{J}}(\tilde{\boldsymbol{x}})$ can be computed as

$$\tilde{\boldsymbol{J}}(\tilde{\boldsymbol{x}}) = \partial_{\tilde{\boldsymbol{x}}} \tilde{\boldsymbol{r}}(\tilde{\boldsymbol{x}}) = \partial_{\tilde{\boldsymbol{x}}} \partial_{\tilde{\boldsymbol{x}}} \boldsymbol{\mathcal{L}}(\tilde{\boldsymbol{x}}) = \begin{bmatrix} \partial_{\boldsymbol{\Phi}} \partial_{\boldsymbol{\Phi}} \mathcal{L}(\tilde{\boldsymbol{x}}) & \partial_{\boldsymbol{\Phi}} \partial_{\boldsymbol{\nu}} \mathcal{L}(\tilde{\boldsymbol{x}}) \\ \partial_{\boldsymbol{\nu}} \partial_{\boldsymbol{\Phi}} \mathcal{L}(\tilde{\boldsymbol{x}}) & \mathbf{0} \end{bmatrix},$$

where

$$\partial_{\boldsymbol{\Phi}} \partial_{\boldsymbol{\Phi}} \mathcal{L}(\tilde{\boldsymbol{x}}) = \partial_{\boldsymbol{\Phi}} \partial_{\boldsymbol{\Phi}} E_h(\boldsymbol{\Phi}) - \nu_A \partial_{\boldsymbol{\Phi}} \partial_{\boldsymbol{\Phi}} A_h(\boldsymbol{\Phi}) - \nu_V \partial_{\boldsymbol{\Phi}} \partial_{\boldsymbol{\Phi}} V_h(\boldsymbol{\Phi}) - \nu_M \partial_{\boldsymbol{\Phi}} \partial_{\boldsymbol{\Phi}} M_h(\boldsymbol{\Phi}),$$

$$\partial_{\boldsymbol{\Phi}} \partial_{\boldsymbol{\nu}} \mathcal{L}(\tilde{\boldsymbol{x}}) = \left[\partial_{\boldsymbol{\Phi}} A_h(\boldsymbol{\Phi}) \; \partial_{\boldsymbol{\Phi}} V_h(\boldsymbol{\Phi}) \; \partial_{\boldsymbol{\Phi}} M_h(\boldsymbol{\Phi}) \right],$$

and

$$\partial_{\boldsymbol{\nu}} \partial_{\boldsymbol{\Phi}} \mathcal{L}(\tilde{\boldsymbol{x}}) = \left[\partial_{\boldsymbol{\Phi}} \partial_{\boldsymbol{\nu}} \mathcal{L}(\tilde{\boldsymbol{x}}) \right]^T.$$

The gradient $\tilde{\boldsymbol{r}}_A(\boldsymbol{\Phi}, \boldsymbol{\nu}) = \partial_{\boldsymbol{\Phi}} \mathcal{L}_A(\boldsymbol{\Phi}, \boldsymbol{\nu})$ and the hessian $\tilde{\boldsymbol{J}}_A(\boldsymbol{\Phi}, \boldsymbol{\nu}) = \partial_{\boldsymbol{\Phi}} \partial_{\boldsymbol{\Phi}} \mathcal{L}_A(\boldsymbol{\Phi}, \boldsymbol{\nu})$ of the augmented Lagrangian with respect to the phase-field nodal values are

$$\begin{aligned} \tilde{\boldsymbol{r}}_A(\boldsymbol{\Phi}, \boldsymbol{\nu}) = \partial_{\boldsymbol{\Phi}} E_h(\boldsymbol{\Phi}) &- \left[\nu_A - \frac{A_h(\boldsymbol{\Phi}) - A_0}{\mu} \right] \partial_{\boldsymbol{\Phi}} A_h(\boldsymbol{\Phi}) \\ &- \left[\nu_V - \frac{V_h(\boldsymbol{\Phi}) - V_0}{\mu} \right] \partial_{\boldsymbol{\Phi}} V_h(\boldsymbol{\Phi}) - \left[\nu_M - \frac{M_h(\boldsymbol{\Phi}) - M_0}{\mu} \right] \partial_{\boldsymbol{\Phi}} M_h(\boldsymbol{\Phi}), \end{aligned}$$

and

$$\begin{aligned} \tilde{\boldsymbol{J}}_A(\boldsymbol{\Phi}, \boldsymbol{\nu}) = \partial_{\boldsymbol{\Phi}} \partial_{\boldsymbol{\Phi}} E_h(\boldsymbol{\Phi}) &+ \frac{1}{\mu} \partial_{\boldsymbol{\Phi}} A_h(\boldsymbol{\Phi}) \otimes \partial_{\boldsymbol{\Phi}} A_h(\boldsymbol{\Phi}) + \frac{1}{\mu} \partial_{\boldsymbol{\Phi}} V_h(\boldsymbol{\Phi}) \otimes \partial_{\boldsymbol{\Phi}} V_h(\boldsymbol{\Phi}) \\ &+ \frac{1}{\mu} \partial_{\boldsymbol{\Phi}} M_h(\boldsymbol{\Phi}) \otimes \partial_{\boldsymbol{\Phi}} M_h(\boldsymbol{\Phi}) - \left[\nu_A - \frac{A_h(\boldsymbol{\Phi}) - A_0}{\mu} \right] \partial_{\boldsymbol{\Phi}} \partial_{\boldsymbol{\Phi}} A_h(\boldsymbol{\Phi}). \end{aligned}$$

With the above expressions, the Newton-Raphson iterations follow directly,

$$\boldsymbol{\Phi}^{n+1} = \boldsymbol{\Phi}^n - \left[\tilde{\boldsymbol{J}}_A(\boldsymbol{\Phi}^n, \boldsymbol{\nu}^n) \right]^{-1} \tilde{\boldsymbol{r}}_A(\boldsymbol{\Phi}^n, \boldsymbol{\nu}^n)$$

in the first stage described in Section 3.2, and

$$\tilde{\boldsymbol{x}}^{n+1} = \tilde{\boldsymbol{x}}^n - \left[\tilde{\boldsymbol{J}}(\tilde{\boldsymbol{x}}^n) \right]^{-1} \tilde{\boldsymbol{r}}(\tilde{\boldsymbol{x}}^n)$$

in the second stage.

Table B.6: Description of the uniform and adapted grids used in the calculations.

ID	Grid	# nodes	Features
O1	Uniform	6124	$\bar{h} = 0.024$
O11	Adapted	6124	CVT starting from grid O1, with $f = 10$, and $\mathbf{\Phi}$ for $\epsilon = 0.04$
O12	Adapted	6124	CVT starting from grid O11, with $f = 100$, and $\mathbf{\Phi}$ for $\epsilon = 0.03$
O13	Adapted	6124	CVT starting from grid O12, with $f = 1000$, and $\mathbf{\Phi}$ for $\epsilon = 0.025$
O2	Uniform	12271	$\bar{h} = 0.017$
O21	Adapted	12271	CVT starting from grid O2, with $f = 10$, and $\mathbf{\Phi}$ for $\epsilon = 0.03$
O22	Adapted	12271	CVT starting from grid O21, with $f = 100$, and $\mathbf{\Phi}$ for $\epsilon = 0.025$
O23	Adapted	12271	CVT starting from grid O22, with $f = 1000$, and $\mathbf{\Phi}$ for $\epsilon = 0.015$
O3	Uniform	24597	$\bar{h} = 0.012$
O31	Adapted	24597	CVT starting from grid O3, with $f = 10$, and $\mathbf{\Phi}$ for $\epsilon = 0.03$
O32	Adapted	24597	CVT starting from grid O31, with $f = 100$, and $\mathbf{\Phi}$ for $\epsilon = 0.015$
O7	Uniform	296344	$\bar{h} = 0.0034$
P1	Uniform	6124	$\bar{h} = 0.024$
P11	Adapted	6124	CVT starting from grid P1, with $f = 10$, and $\mathbf{\Phi}$ for $\epsilon = 0.04$
P12	Adapted	6124	CVT starting from grid P11, with $f = 100$, and $\mathbf{\Phi}$ for $\epsilon = 0.03$
P13	Adapted	6124	CVT starting from grid P12, with $f = 1000$, and $\mathbf{\Phi}$ for $\epsilon = 0.025$
P7	Uniform	296344	$\bar{h} = 0.0034$

Appendix B. Progressive refinement of the grid

Table B.6 provides details about the progressive refinement of the grids presented in the paper. The adaptive process produces non-uniform nodal distributions. We use the nodal spacing as figure to measure the non-uniformity of a grid. The nodal spacing h_a can be understood as the average distance from a specific node $\boldsymbol{x}_a$ to the first ring of nearest neighbors $\boldsymbol{x}_b$, and it can be easily estimated with the information provided by the CVT. Indeed, as for a specific Voronoi cell Ω_a (associated to a node $\boldsymbol{x}_a$) we know all its adjacent Voronoi cells Ω_b (and thus the first ring of nodes $\boldsymbol{x}_b$), a good estimation of h_a can be obtained by computing the average distance among the node $\boldsymbol{x}_a$ and all its neighbors $\boldsymbol{x}_b$. The nodal spacing is also required to compute the basis functions (see Section 3.1) and to determine the transition parameter ϵ_{min}, as we explain later.

In Figure B.11 we illustrate the histograms for the nodal spacing distribution of uniform and adapted grids of 6,124 points corresponding to the discocyte equilibrium shape (see Table B.6 for the features of each grid). To facilitate the comparison between the different grids, we substract the nodal spacing of the uniform grid, i.e. $\bar{h} = 0.024$, to the nodal spacing of all the histograms. The top-left histogram corresponds to O1, and is strongly concentrated around zero because the grid is almost perfectly uniform. The other three histograms show the nodal spacing distribution for the adapted grids O11, O12 and O13. Note that the distributions exhibit two peaks, one associated to the smallest nodal spacing and the other to the largest one. The location and amplitude of these peaks change as the adaptivity algorithm concentrates further the nodes in a thin region near the interface (see Figure 7). The peak of the left increases its magnitude and becomes narrower, which means that the smallest nodal spacing decreases and a larger fraction

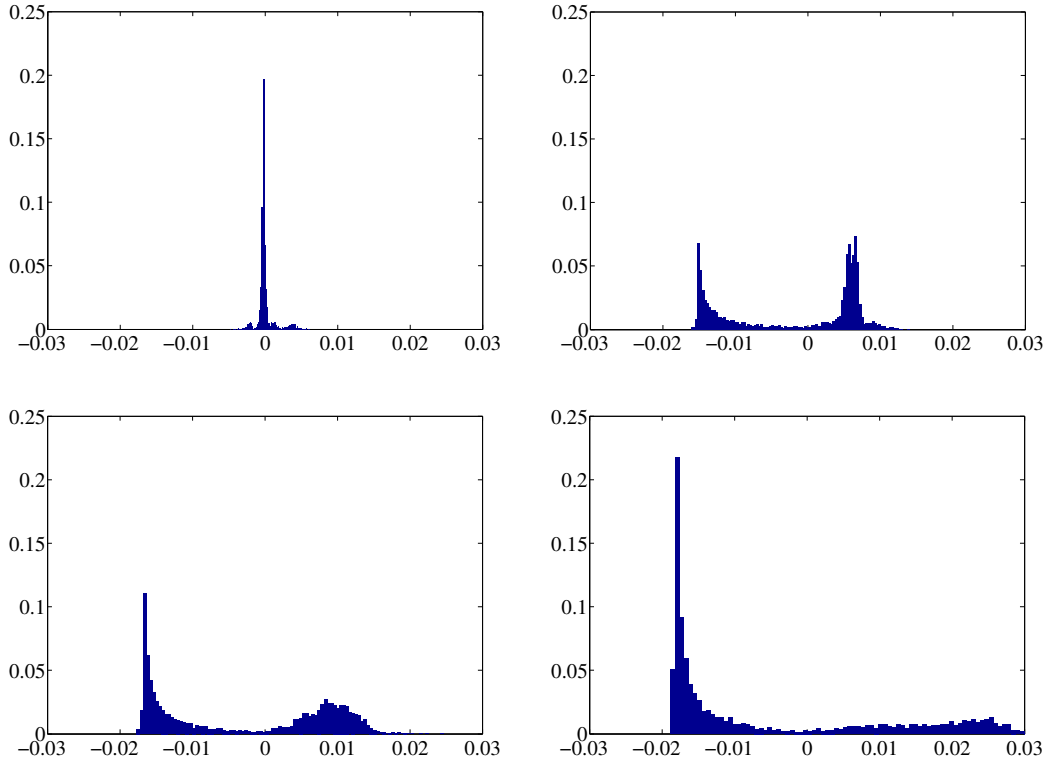

Figure B.11: Histograms of the nodal spacing distribution for different grids of 6124 points (discocyte equilibrium shape). The histograms are centered in $\bar{h} = 0.024$ and correspond to grids O1 (top-left), O11 (top-right), O12 (bottom-left) and O13 (bottom-right).

of the nodes is in the refined region. The peak of the right decreases its magnitude and becomes widespread, as fewer nodes suffice to describe the coarse region. The value of ϵ_{min} that a given grid can resolve is computed from the criterion $\epsilon_{min} \geq 2h_{min}$, where h_{min} is the nodal spacing of the left peak.

[1] M. Karlsson, K. Sott, M. Davidson, A.-S. Cans, P. Linderholm, D. Chiu, O. Orwar, Formation of geometrically complex lipid nanotube-vesicle networks of higher-order topologies, Proceedings of the National Academy of Sciences 99 (18) (2002) 11573–11578.

[2] M. Edidin, Lipids on the frontier: a century of cell-membrane bilayers, Nature Reviews Molecular Cell Biology 4 (5) (2003) 414–418.

[3] S. Semrau, T. Schmidt, Membrane heterogeneity – from lipid domains to curvature effects, Soft Matter 5 (17) (2009) 3174–3186.

[4] U. Seifert, Configurations of fluid membranes and vesicles, Advances in Physics 46 (1) (1997) 13–137.

[5] E. Reimhult, F. Höök, B. Kasemo, Intact vesicle adsorption and supported biomembrane formation from vesicles in solution: influence of surface chemistry, vesicle size, temperature, and osmotic pressure, Langmuir 19 (5) (2003) 1681–1691.

[6] M. K. W. Wintz, U. Seifert, R. Lipowsky, Fluid vesicles in shear flow, Physical Review Letters 77 (17) (1996) 3685–3688.

[7] L.-T. Gao, X.-Q. Feng, H. Gao, A phase field method for simulating morphological evolution of vesicles in electric fields, Journal of Computational Physics 228 (2009) 4162–4181.

[8] T. Baumgart, S. Hess, W. Webb, Imaging coexisting fluid domains in biomembrane models coupling curvature and line tension, Nature 425 (2003) 821–824.

[9] E. Lindahl, O. Edholm, Mesoscopic undulations and thickness fluctuations in lipid bilayers from molecular dynamics simulations, Biophysical Journal 79 (2000) 426–433.

[10] B. Reynwar, G. Illya, V. Harmandaris, M.M.Müller, K. Kremer, M. Deserno, Aggregation and vesiculation of membrane proteins by curvature-mediated interactions, Nature 447 (2007) 461–464.

[11] I. Cooke, K. Kremer, M. Deserno, Tunable generic model for fluid bilayer membranes, Physical Review E 72 (2005) 011506.

[12] H. Noguchi, G. Gompper, Dynamics of fluid vesicles in shear flow: Effect of membrane viscosity and thermal fluctuations, Physical Review E 72 (2005) 011901.

[13] S. Svetina, B. Zeks, Bilayer couple hypothesis of red cell shape transformations and osmotic hemolysis, Biochim. Biophys. Acta 42 (1983) 86–90.

[14] F. Julicher, R. Lipowsky, Shape transformations of vesicles with intermembrane domains, Physical Review E 53 (3) (1996) 2670–2683.

[15] U. Seifert, S. A. Langer, S. A., Viscous modes of fluid bilayer membranes, Europhysics Letters 23 (1) (1993) 71–76.

[16] P. Sens, Dynamics of nonequilibrium bud formation, Physical Review Letters 93 (10) (2004) 108103.

[17] M. Arroyo, A. DeSimone, Relaxation dynamics of fluid membranes, Phys. Rev. E 79 (3) (2009) 031915.

[18] M. Rahimi, M. Arroyo, Shape dynamics, lipid hydrodynamics, and the complex viscoelasticity of bilayer membranes, Physical Review E 86 (2012) 011932.

[19] P. Canham, The minimum energy of bending as a possible explanation of the biconcave shape of the human red blood cell, Journal of Theoretical Biology 26 (1) (1970) 61–81.

[20] W. Helfrich, Elastic properties of lipid bilayers: theory and possible experiments, Z. Naturforsch C 28 (11) (1973) 693–703.

[21] F. Feng, W. Klug, Finite element modeling of lipid bilayer membranes, Journal of Computational Physics 220 (1) (2006) 394–408.

[22] S. Veerapaneni, A. Rahimian, G. Biros, D. Zorin, A fast algorithm for simulating vesicle flows in three dimensions, Journal of Computational Physics 230 (2011) 5610–5634.

[23] Q. Du, C. Liu, X. Wang, A phase field approach in the numerical study of the elastic bending energy for vesicle membranes, Journal of Computational Physics 198 (2004) 450–468.

[24] T. Biben, K. Kassner, C. Misbah, Phase-field approach to three-dimensional vesicle dynamics, Physical Review E 72 (4) (2005) 041921.

[25] F. Campelo, Modeling morphological instabilities in lipid membranes with anchored amphiphilic polymers, J. Chem. Biol. 2 (2009) 65–80.

[26] M. Arroyo, M. Ortiz, Local maximum-entropy approximation schemes: a seamless bridge between finite elements and meshfree methods, International Journal for Numerical Methods in Engineering 65 (13) (2006) 2167–2202.

[27] C. Peco, A. Rosolen, M. Arroyo, An adaptive meshfree method for phase-field models of biomembranes. Part II: a Lagrangian approach for membranes in viscous fluids, Journal of Computational Physics ?? (2013) ??–??

[28] L. Ma, W. Klug, Viscous regularization and r-adaptive remeshing for finite element analysis of lipid membrane mechanics, Journal of Computational Physics 227 (11) (2008) 5816 – 5835.

[29] C. Elliott, B. Stinner, Modeling and computation of two phase geometric biomembranes using surface finite elements, Journal of Computational Physics 229 (18) (2010) 6585–6612.

[30] A. Bonito, R. Nochetto, S. Pauletti, Parametric FEM for geometric biomembranes, Journal of Computational Physics 229 (9) (2010) 3171–3188.

[31] L. Landau, On the theory of phase transitions, Gordon and Breach, 1937.

[32] R. Sekerka, Morphology: from sharp interface to phase field models, Journal of Crystal Growth 264 (2004) 530–540.

[33] I. Steinbach, Phase-field models in materials science, Modelling and Simulation in Materials Science and Engineering 17 (2009) 073001.

[34] G. Francfort, J.-J. Marigo, Revisiting brittle fracture as an energy minimization problem, Journal of the Mechanics and Physics of Solids 46 (1998) 1319–1342.

[35] C. Miehe, F. Welschinger, M. Hofacker, Thermodynamically consistent phase-field models of fracture: Variational principles and multi-field fe implementations, International Journal for Numerical Methods in Engineering 83 (2010) 1273–1311.

[36] A. Abdollahi, I. Arias, Phase-field modeling of the coupled microstructure and fracture evolution in ferroelectric single crystals, Acta Materialia 59 (12) (2011) 4733–4746.

[37] A. Rätz, A. Ribalta, A. Voigt, Surface evolution of elastically stressed films under deposition by a diffuse interface model, Journal of Computational Physics 214 (2006) 187–208.

[38] M. Benes, V. Chalupecky, K. Mikula, Geometrical image segmentation by the Allen-Cahn equation, Applied Numerical Mathematics 51 (2004) 187–205.

[39] D. Jacqmin, Calculation of two-phase Navier-Stokes flows using phase-field modeling, Journal of Computational Physics 155 (1999) 96–127.

[40] X. Wang, Phase field models and simulations of vesicle bio-membranes, Ph.D. thesis, Department of Mathematics, The Pennsylvania State University, Pennsylvania, USA (2005).

[41] G. Bellettini, L. Mugnai, Approximation of Helfrich's functional via diffuse interfaces, SIAM Journal on Mathematical Analysis 42 (2010) 2402–2433.

[42] Q. Du, Phase field calculus, curvature-dependent energies, and vesicle membranes, Philosophical Magazine 91 (2010) 165–181.

[43] Q. Du, C. Liu, R. Ryham, X. Wang, Energetic variational approaches in modeling vesicle and fluid interactions, Physica D 238 (2009) 923–930.

[44] F. Campelo, Shapes in Cells. Dynamic instabilities, morphology, and curvature in biological membranes, Ph.D. thesis, Universitat de Barcelona (2008).

[45] J. Lowengrub, A. Rätz, A. Voigt, Phase-field modeling of the dynamics of multicomponent vesicles: Spinodal decomposition, coarsening, budding, and fission, Physical Review E 79 (2009) 031926.

[46] T. Hughes, J. Cottrell, Y. Bazilevs, Isogeometric analysis: CAD, finite elements, NURBS, exact geometry and mesh refinement, Computer Methods in Applied Mechanics and Engineering 194 (2005) 4135–4195.

[47] H. Gomez, V. Calo, Y. Bazilevs, T. Hughes, Isogeometric analysis of the Cahn-Hilliard phase-field model, Computer Methods in Applied Mechanics and Engineering 197 (2008) 4333–4352.

[48] H. Gomez, T. Hughes, X. Nogueira, V. Calo, Isogeometric analysis of the isothermal Navier-Stokes-Korteweg equations, Computer Methods in Applied Mechanics and Engineering 199 (2010) 1828–1840.

[49] Q. Du, L. Zhu, Analysis of a mixed finite element method for a phase field bending elasticity model of vesicle membrane deformation, Journal of Computational Mathematics 24 (2006) 265–280.

[50] Q. Du, J. Zhang, Adaptive finite element method for a phase field bending elasticity model of vesicle membrane deformations, SIAM J. Sci. Comput. 30 (3) (2008) 1634–1657.

[51] H. Ceniceros, R. Nós, A. Roma, Three-dimensional, fully adaptive simulations of phase-field fluid models, Journal of Computational Physics 229 (2010) 6135–6155.

[52] S. Wise, J. Kim, J. Lowengrub, Solving the regularized, strongly anisotropic Cahn–Hilliard equation by an adaptive nonlinear multigrid method, Journal of Computational Physics 226 (1) (2007) 414–446.

[53] W. Feng, P. Yu, S. Hu, Z. Liu, Q. Du, L. Chen, A Fourier spectral moving mesh method for the Cahn-Hilliard equation with elasticity, Communications in Computational Physics 5 (2–4) (2009) 582–599.

[54] A. Voigt, T. Witkowski, Hybrid parallelization of an adaptive finite element code, KYBERNETIKA 46 (2010) 316–327.

[55] P. Yue, C. Zhou, J. Feng, C. Ollivier-Gooch, H. Hu, Phase-field simulations of interfacial dynamics in viscoelastic fluids using finite elements with adaptive meshing, Journal of Computational Physics 219 (1) (2006) 47–67.

[56] C. Zhou, P. Yue, J. Feng, C. Ollivier-Gooch, H. Hu, 3d phase-field simulations of interfacial dynamics in Newtonian and viscoelastic fluids, Journal of Computational Physics 229 (2010) 498–511.

[57] L. Cueto-Felgueroso, J. Peraire, A time-adaptive finite volume method for the Cahn-Hilliard and Kuramoto-Sivashinsky equations, Journal of Computational Physics 227 (2008) 9985–10017.

[58] R. Braun, B. Murray, Adaptive phase-field computations of dendritic crystal growth, Journal of Crystal Growth 177 (1997) 41–53.

[59] J. Rosam, P. Jimack, A. Mullis, A fully implicit, fully adaptive time and space discretisation method for phase-field simulation of binary alloy solidification, Journal of Computational Physics 225 (2007) 1271–1287.

[60] W. Feng, P. Yu, S. Hu, Z. Liu, Q. Du, L. Chen, Spectral implementation of an adaptive moving mesh method for phase-field equations, Journal of Computational Physics 220 (1) (2006) 498–510.

[61] C. Lan, Y. Chang, Efficient adaptive phase field simulation of directional solidification of a binary alloy, Journal of Crystal Growth 250 (2003) 525–537.

[62] Z. Tan, K. Lim, B. Khoo, An adaptive mesh redistribution method for the incompressible mixture flows using phase-field model, Journal of Computational Physics 225 (2007) 1137–1158.

[63] D. Millán, A. Rosolen, M. Arroyo, Nonlinear manifold learning for meshfree finite deformation thin shell analysis, International Journal for Numerical Methods in Engineering 93 (7) (2013) 685–713.

[64] D. Millán, A. Rosolen, M. Arroyo, Thin shell analysis from scattered points with maximum-entropy approximants, International Journal for Numerical Methods in Engineering 85 (6) (2011) 723–751.

[65] C. Cyron, M. Arroyo, M. Ortiz, Smooth, second order, non-negative meshfree approximants selected by maximum entropy, International Journal for Numerical Methods in Engineering 79 (13) (2009) 1605–1632.

[66] A. Rosolen, D. Millán, M. Arroyo, Second order convex *maximum entropy* approximants with applications to high order PDE, International Journal for Numerical Methods in Engineering 94 (2) (2013) 150–182.

[67] Q. Du, V. Faber, M. Gunzburger, Centroidal Voronoi Tessellations: Applications and Algorithms, SIAM Review 41 (4) (1999) 637–676.

[68] P. Lancaster, K. Salkauskas, Surfaces generated by moving least squares methods, Mathematics of Computation 37 (155) (1981) 141–158.

[69] N. Sukumar, Construction of polygonal interpolants: a maximum entropy approach, International Journal for Numerical Methods in Engineering 61 (12) (2004) 2159–2181.

[70] F. Cirak, M. Ortiz, P. Schröder, Subdivision surfaces: a new paradigm for thin-shell finite-element analysis, International Journal for Numerical Methods in Engineering 47 (12) (2000) 2039–2072.

[71] A. Rosolen, D. Millán, M. Arroyo, On the optimum support size in meshfree methods: a variational adaptivity approach with maximum entropy approximants, International Journal for Numerical Methods in Engineering 82 (7) (2010) 868–895.

[72] A. Conn, N. Gould, P. Toint, A globally convergent augmented Lagrangian algorithm for optimization with general constraints and simple bounds, SIAM J. Numer. Anal. 28 (2) (1991) 545–572.

[73] J. Nocedal, S. Wright, Numerical Optimization, Springer, USA, 1999.

[74] J.-S. Chen, C.-T. Wu, S. Yoon, Y. You, A stabilized conforming nodal integration for galerkin mesh-free methods, International Journal for Numerical Methods in Engineering 50 (2) (2001) 435–466.

[75] U. Seifert, K. Berndl, R. Lipowsky, Shape transformations of vesicles-phase-diagram for spontaneous-curvature and bilayer-coupling models, Physical Review A 44 (2) (1991) 1182–1202.